Biophysical Journal
Article

Biophysical Society

Molecular Mechanisms of Tight Binding through Fuzzy Interactions

Qingliang Shen,[1] Jie Shi,[2] Danyun Zeng,[1] Baoyu Zhao,[1] Pingwei Li,[1] Wonmuk Hwang,[2,3,4,*] and Jae-Hyun Cho[1,*]
[1]Department of Biochemistry and Biophysics, [2]Department of Biomedical Engineering, and [3]Department of Materials Science and Engineering, Texas A&M University, College Station, Texas; and [4]School of Computational Sciences, Korea Institute for Advanced Study, Seoul, South Korea

ABSTRACT Many intrinsically disordered proteins (IDPs) form fuzzy complexes upon binding to their targets. Although many IDPs are weakly bound in fuzzy complexes, some IDPs form high-affinity complexes. One example is the nonstructural protein 1 (NS1) of the 1918 Spanish influenza A virus, which hijacks cellular CRKII through the strong binding affinity (K_d ~10 nM) of its proline-rich motif (PRM^{NS1}) to the N-terminal Src-homology 3 domain of CRKII. However, its molecular mechanism remains elusive. Here, we examine the interplay between structural disorder of a bound PRM^{NS1} and its long-range electrostatic interactions. Using x-ray crystallography and NMR spectroscopy, we found that PRM^{NS1} retains substantial conformational flexibility in the bound state. Moreover, molecular dynamics simulations showed that structural disorder of the bound PRM^{NS1} increases the number of electrostatic interactions and decreases the mean distances between the positively charged residues in PRM^{NS1} and the acidic residues in the N-terminal Src-homology 3 domain. These results are analyzed using a polyelectrostatic model. Our results provide an insight into the molecular recognition mechanism for a high-affinity fuzzy complex.

INTRODUCTION

There is growing interest in understanding molecular recognition mechanisms between proline-rich motifs (PRMs) and their cognate domains such as Src-homology 3 (SH3) domains because PRM is one of the most common linear motifs in the eukaryotic proteome (1,2). PRMs are also highly enriched in intrinsically disordered proteins (IDPs) or intrinsically disordered regions (IDRs) (3). Although they lack stable conformations, IDPs/IDRs mediate protein-protein interactions in signal transduction or transcription regulation (4–6). Hence, it is of importance to understand the molecular mechanisms determining the binding affinity and selectivity of IDRs. Recent studies have shown that some IDPs/IDRs retain substantial conformational flexibility even in a complex with their binding partner. This mode of complex was described as a fuzzy complex (7). Given the growing importance of fuzzy complexes in biological processes, elucidating their molecular recognition mechanism is essential.

The nonstructural protein 1 (NS1) of influenza A viruses (IAVs) plays an important role in suppressing the antiviral immune responses of host cells (8,9). Unlike common seasonal IAVs, the 1918 Spanish IAV uses NS1 to hijack cellular signaling adaptor CRKII (10). Recently, we have shown that the viral hijacking occurs because a PRM in the NS1 binds to the N-terminal SH3 (nSH3) domain of CRK with an exceptionally high affinity (11). The binding affinity of the nSH3 domain with PRM^{NS1} is significantly higher than its interactions with other cellular binding partners. For example, the nSH3 domain binds PRM^{NS1} with ~3000-fold higher affinity than the PRM of JNK1 (11,12). It was suggested that the high affinity is due to long-range electrostatic interactions between positively charged residues in PRM^{NS1} and a negatively charged binding interface in the nSH3 domain (11). However, the molecular mechanism by which long-range electrostatic interactions increase the affinity of PRM^{NS1} to the nSH3 domain remains elusive.

Long-range electrostatic interactions play important roles in the molecular recognition in fuzzy complexes (13,14). Borg et al. (15) proposed a polyelectrostatic model, in which multiple charges in an IDP increase its binding affinity to a rigid partner through nonspecific, long-range electrostatic interactions as a binding mechanism of a fuzzy complex. In this model, fuzzy complexes undergo fast conformational exchanges between multiple conformations, interacting with a folded partner through long-range electrostatic interactions.

Submitted November 3, 2017, and accepted for publication January 29, 2018.

*Correspondence: hwm@tamu.edu or jaehyuncho@tamu.edu
Qingliang Shen and Jie Shi contributed equally to this work.

Editor: Monika Fuxreiter.
https://doi.org/10.1016/j.bpj.2018.01.031

Here, we provide evidence that PRM^{NS1} retains its conformational flexibility when complexed with the nSH3 domain, indicating a fuzzy complex. In addition, we present the contribution of long-range electrostatic interactions and a detailed structural mechanism by which long-range electrostatics can increase the binding affinity of PRM^{NS1} to the nSH3 domain. We obtained these results using a combination of x-ray crystallography, NMR dynamics experiments, and molecular dynamics (MD) simulation. We find that structural disorder of the bound PRM^{NS1} plays a key role in mediating the long-range, nonspecific electrostatic interactions with the nSH3 domain.

MATERIALS AND METHODS

Protein and peptides

All protein samples for crystallization, fluorescence, and NMR experiments were prepared as described elsewhere (12). Synthetic peptides were purchased in a crude form and further purified using reverse-phase high-performance liquid chromatography in our laboratory. The amino acid sequence of PRM^{NS1} is YG_{210}RPPLPPKQKRK$_{221}$. The N- and C-termini of peptides were acetylated and amidated, respectively. The peptide concentration was determined by measuring the ultraviolet absorption at 280 nm of a single tyrosine at the N-terminal end of the peptide. The isotope-labeled PRM^{NS1} contained an additional Gly residue at the C-terminus to prevent proteolysis during bacterial expression and purification. Based on our structure, we assumed that one additional Gly at the C-terminus does not affect the structure and dynamics of PRM^{NS1} substantially.

Crystallization and structure determination

Four millimolar nSH3 was mixed with 5 mM PRM^{NS1} for the crystallization trials. The sample was crystallized by the hanging drop vapor diffusion method in 0.1 M sodium acetate (pH 4.6), 30% PEG 2000, and 0.2 M ammonium sulfate, which is the duplicate of the previous crystallization condition (Protein Data Bank (PDB): 5UL6) for the nSH3:PRM^{NS1} complex. A 1.75 Å resolution data set was collected at 120 K using an R-AXIS IV^{2+} image plate detector mounted on a Rigaku MicroMax 007HF x-ray generator (Rigaku, The Woodlands, TX). The data were processed using iMosflm in the CCP4 package (16). The structure was determined using the nSH3 domain model (PDB: 5UL6) as a search model and the Phenix software suite (17). The NS1 PRM peptide was modeled into the difference map manually in COOT (18) and refined with Phenix. The electrostatic potential surface of nSH3 domain was calculated using APBS and PDB: 2PQR (19–21).

NMR spectroscopy

All NMR experiments were conducted using protein samples in 20 mM sodium phosphate (pH 6.1), 80 mM NaCl, 0.02% sodium azide, 1 mM EDTA, 10 μM DSS (4,4-dimethyl-4-silapentane-sulfonate), and 10% D_2O at 25°C. NMR data for PRM^{NS1} were acquired using a sample containing isotope-labeled PRM^{NS1} (490 μM) and nonlabeled nSH3 domain (500 μM). NMR data for the nSH3 domain were acquired using a sample containing isotope-labeled nSH3 domain (320 μM) and nonlabeled PRM^{NS1} (350 μM). The temperature-dependent heteronuclear single quantum coherence (HSQC) spectra were acquired using a Bruker 500 MHz spectrometer (Bruker, Billerica, MA). Each spectrum was acquired with 64 scans per t1 point. The temperatures of NMR samples were calibrated using deuterated methanol-d_4 (22). The assignment of backbone ^1H, ^{13}C, ^{15}N resonances was carried out using Bruker 600 and 800 MHz spectrometers, as described elsewhere (12). NMR spectra were processed with NMRPipe (23) and analyzed with NMRViewJ (One Moon Scientific, Westfield, NJ) and CARA (24).

Measurement of NMR relaxation parameters

All relaxation parameters were measured at 25°C using a Bruker 600 MHz spectrometer. For the heteronuclear nuclear Overhauser effect (NOE) measurements, a recycle delay of 12 s was used in the reference experiment. The saturation of proton during the steady state was performed by applying 180° pulses for 4 s (25). For R_2 measurement, a recycle delay of 2 s was used between transitions. Errors of the relaxation parameters were estimated using duplicated measurements.

MD simulation

Simulations were performed using CHARMM version 40a1 with param36 all-atom force field (26,27). An initial energy optimization was carried out for 1600 steps (with 400 steps using the steepest descent method and 1200 steps using the adopted basis Newton-Raphson method) in the generalized Born with a simple switching implicit solvent (28). The protein complex was solvated using the TIP3P water model and electrically neutralized with Cl^- and Na^+ ions. The system was heated from 0 to 300 K for 100 ps and then equilibrated for 160 ps under the constant number, pressure, temperature ensemble at 1 atm and 300 K. Production runs were performed under the constant number, volume, temperature ensemble at 300 K.

Cluster analysis

With backbone heavy atoms in the nSH3 domain as a positional reference, PRM^{NS1} conformations from the MD trajectories were analyzed using a cluster analysis (29). Agglomerative hierarchical clustering was used based on the similarity between different conformations, which is measured as the squared Euclidean distance of the backbone heavy atoms in PRM^{NS1}. The average linkage was chosen to measure intercluster similarity, which is the average of all pairwise similarities between observations in two clusters. The representative conformation of each cluster was chosen to have the smallest root-mean-square deviation from the calculated average structure for the cluster.

Binding assay

The dissociation constants (K_d) of nSH3:PRM complexes were measured by monitoring the change of tryptophan fluorescence signal. The excitation wavelength was 295 nm. All binding assays were performed in a stirred 1-cm-path-length cuvette using a PTI QM-400 fluorimeter. The protein concentration used for the fluorescence-based binding assays was 0.1 μM. The measurements were done in 20 mM sodium phosphate (pH 6.1) and either 80 mM or 1 M NaCl at 25°C. The K_d was calculated by assuming a 1:1 complex and by the global fitting of the repeatedly measured fluorescence intensities to Eq. 1:

$$\Delta F = \Delta F_{\max}\left(\frac{[P_t]+[L_t]+K_d \pm \sqrt{([P_t]+[L_t]+K_d)^2-4[P_t][L_t]}}{2[P_t]}\right), \quad (1)$$

where ΔF and ΔF_{max} are the change and the maximum amplitude of signal change, respectively. P_t is the total protein concentration and L_t is the total ligand concentration at each titration point. The reported K_d values are the average of two repeated measurements.

RESULTS AND DISCUSSION

Long-range electrostatic interaction increases the binding affinity of nSH3:PRM^{NS1} complex

It was previously suggested that positively charged residues, particularly in the C-terminal region of PRM^{NS1}, interact with a large negatively charged surface of the nSH3 domain through long-range electrostatic interactions (11). To directly test the contribution of long-range electrostatics in increasing the binding affinity, we measured K_d values of the nSH3:PRM^{NS1} complex in the presence of 80 mM and 1 M NaCl. The K_d increased by more than 100-fold in the presence of 1 M NaCl, compared to that in the presence of 80 mM NaCl (Fig. 1).

We attributed the large decrease in the affinity to the screening of long-range electrostatics in the complex. The Debye screening lengths are 10.7 and 3.0 Å in the solution, with ionic strengths of 80 mM and 1 M, respectively. Hence, long-range interactions are screened in a high ionic strength solution, whereas the short-range electrostatic interactions within 3 Å remain effective under the same condition. Indeed, our previous crystal structure indicated that the distances of all short-range electrostatic interactions in the nSH3:PRM^{NS1} are within 3 Å (Fig. S1). Moreover, all these short-range electrostatic interactions in the nSH3:PRM^{NS1} complex are well-conserved in the complexes with much weaker affinities (12,30), indicating that these specific salt bridges are not responsible for the unusually high affinity of PRM^{NS1}.

We further examined the effect of the positive charges in PRM^{NS1} on the binding affinity using mutagenesis. We replaced all the C-terminal positively charged residues (K219, R220, and K221) with Gly. We chose Gly to minimize the effect of other types of amino acids on the intrinsic conformational propensity of PRM^{NS1} and to retain the flexibility of the C-terminal region. As expected, the mutant PRM^{NS1} showed significantly lower affinity to the nSH3 domain. Its K_d is 0.9 μM, which is similar to that shown in the presence of 1 M NaCl (Fig. S2). Taken together, these results show that the long-range electrostatic interactions play an important role in increasing the stability of the nSH3:PRM^{NS1} complex.

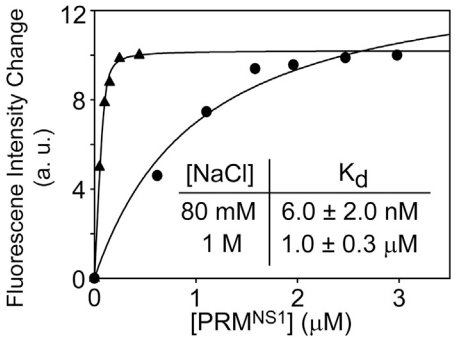

FIGURE 1 Fluorescence-based measurement of binding affinity between the nSH3 domain and PRM^{NS1} in the presence of 80 mM (*triangles*) and 1 M (*circles*) NaCl. The inset shows K_d values from repeated measurements.

New crystal structure displays alternative binding mode of bound PRM^{NS1}

In this study, we determined a new—to our knowledge—crystal structure of the nSH3:PRM^{NS1} complex that displays a different binding mode of PRM^{NS1} from that of the previous structure (Fig. 2; Fig. S3; Table S1). To distinguish the two conformations of PRM^{NS1}, the previous and the current structures are labeled as PRM^{NS1A} and PRM^{NS1B}, respectively. The two complex structures showed similar changes in overall solvent-accessible surface area upon complexation: 923 and 1080 Å^2 for nSH3:PRM^{NS1A} and nSH3:PRM^{NS1B}, respectively. The two bound PRM^{NS1} showed virtually identical structures with respect to the N-terminal region and core PPLPPK motif (Fig. 2 *B*), including all intermolecular short-range electrostatic interactions mediated by K217.

In contrast, the C-terminal regions of bound PRM^{NS1} showed a large conformational difference (Fig. 2 *B*). This is due to large changes in the backbone φ/ψ angles of Q218, from −82.0°/−27.5° in PRM^{NS1A} to −122.9°/176.9° in PRM^{NS1B} (Fig. 2 *B*). This results in drastic changes in the intermolecular interactions mediated by positively charged residues in the C-terminal end of Q218 in PRM^{NS1} (Fig. S4). The most notable change is the exchange of positions between R220 and K219. In PRM^{NS1A}, K219 is the major residue interacting with acidic residues in the RT-loop of the nSH3 domain. In PRM^{NS1B}, R220 occupies the position and K219 is fully exposed to solvent (Fig. 3, *A* and *B*). Another noticeable change is the hydrogen bonds mediated by E166 in the nSH3 domain. E166 forms a

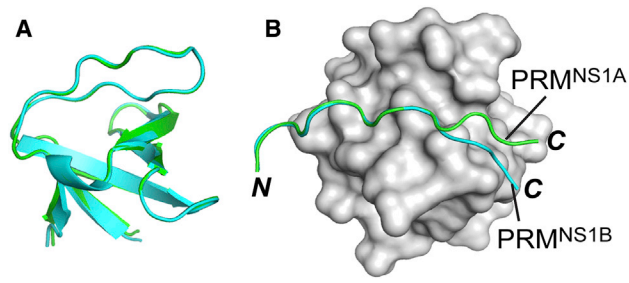

FIGURE 2 Comparison of crystal structures between the nSH3:PRM^{NS1A} (*green*, PDB: 5UL6) and nSH3:PRM^{NS1B} (*cyan*, PDB: 6ATV) complexes. (*A*) shows the overlaid structure of the nSH3 domains. (*B*) shows the overlaid structures of PRM^{NS1A} and PRM^{NS1B}. To see this figure in color, go online.

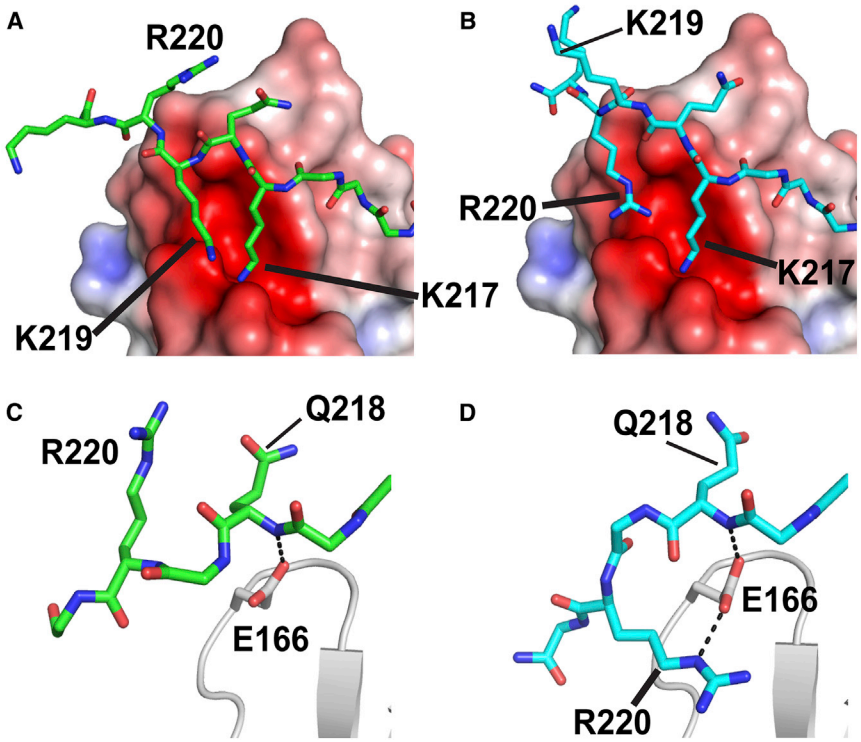

FIGURE 3 Conformational difference in the C-terminal region of bound PRM^{NS1}. The changes in the positions of K219 and R220 in PRM^{NS1A} and PRM^{NS1B} are displayed in (*A*) and (*B*). Hydrogen bonds between E166 of the nSH3 domain (*gray*) and Q218 in PRM^{NS1A} are shown in (*C*), and those between Q218 and R220 in PRM^{NS1B} are shown in (*D*). To see this figure in color, go online.

hydrogen bond with the backbone amide of Q218 in PRM^{NS1A}, but it forms an additional hydrogen bond with the side chain NH^{ε} of R220 in PRM^{NS1B} (Fig. 3, *C* and *D*). These results suggest that the bound PRM^{NS1} may undergo conformational exchange between the two alternative binding modes in solution state.

Structural heterogeneity of PRM^{NS1} probed by NMR spectroscopy

Using NMR spectroscopy, we examined whether the alternative binding of PRM^{NS1} observed by crystallography is populated in solution state. The NMR ^{1}H-^{15}N HSQC spectrum of ^{15}N-PRM^{NS1} bound to the ^{14}N-nSH3 showed that the backbone H^{N} resonance of Q218 shifted significantly downfield (10.47 ppm) because of the hydrogen bond with E166 of the nSH3 as shown in the crystal structures (Figs. 3 *C* and 4 *A*). However, the peak broadened significantly at 25°C, indicating a chemical exchange between alternative conformations in intermediate NMR timescale. When we lowered the temperature of the NMR sample to 6°C, the backbone amide peak of Q218 was split into two peaks, major and minor, indicating that the exchange between the two conformations is in the slow-exchange regime (Fig. 4 *A*). In contrast, other C-terminal residues showed one set of peaks at both 6 and 25°C (Fig. S5).

To examine whether these split peaks correspond to the two crystallographic conformations of PRM^{NS1}, we compared the calculated backbone $^{1}H/^{15}N$ chemical shifts of Q218 in PRM^{NS1A} and PRM^{NS1B} with those of the major and minor peaks observed at 6°C. We used SHIFTX2 for the calculation of chemical shifts from the crystal structures (31). The calculated $^{1}H/^{15}N$ chemical shifts of Q218 were 9.64/122.63 and 9.24/121.58 ppm for PRM^{NS1A} and PRM^{NS1B}, respectively. The differences in the calculated chemical shifts between PRM^{NS1A} and PRM^{NS1B} are comparable to those between the major and minor peaks, although the absolute chemical shifts differ between experimental and calculated values. This indicates that PRM^{NS1A} and PRM^{NS1B} might correspond to minor (downfield-shifted) and major (upfield-shifted) peaks, respectively (*blue peaks* in Fig. 4 *A*).

We also observed that the side-chain NH^{ε} peak of R220 in the bound PRM^{NS1} was split into at least two peaks at 6°C (Fig. 4 *B*). Although we noticed another minor peak besides the two peaks, its intensity was too low for assignment. Hence, it was not considered in this study. The major peak ($H^{\varepsilon} = 7.53$ ppm) shifted more noticeably downfield than the minor peak ($H^{\varepsilon} = 7.34$ ppm). The SHIFTX2 calculation also yielded noticeably different chemical shifts for H^{ε}-R220 in the two crystal structures: 7.26 and 8.09 ppm for PRM^{NS1A} and PRM^{NS1B}, respectively. This is reasonable because the interaction between H^{ε}-R220 and E166 of the nSH3 is present in PRM^{NS1B}, but not in PRM^{NS1A}. However, it should be noted that the chemical shift differences only allow indirect structural inference, and further structural characterization will be required for unambiguous conclusion.

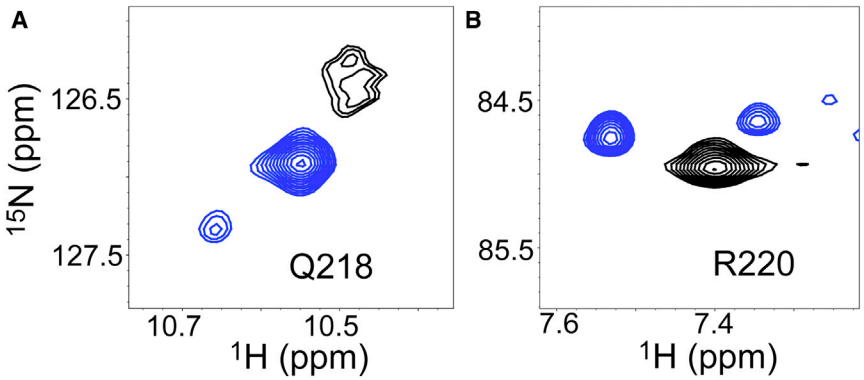

FIGURE 4 ^{1}H-^{15}N HSQC spectra of bound PRM^{NS1}. (*A*) displays the backbone amide resonances of Q218 and (*B*) the side-chain HN$^{\varepsilon}$ resonances of R220 at 25 (*black*) and 6°C (*blue*). To see this figure in color, go online.

For further comparison, we analyzed the intermolecular NOESY spectrum between PRM^{NS1} and the nSH3 domain using ^{15}N-labeled PRM^{NS1} bound to nonlabeled nSH3 domain (Fig. S6). However, the C-terminal residues only showed short-range intramolecular (i.e., within PRM^{NS1}) crosspeaks, which are not characteristic enough for structural comparison with the crystal structures. This result indicates that the C-terminal positively charged residues in PRM^{NS1} remain flexible when undergoing conformational exchange in the slow NMR timescale at 6°C.

Dynamic disorder of PRM^{NS1} probed by NMR spectroscopy and MD simulation

We characterized the conformational flexibility of bound PRM^{NS1} using NMR relaxation experiments. The {^{1}H}-^{15}N heteronuclear NOE reports on backbone dynamics in a picosecond timescale (32). Higher (>0.7) NOE values correspond to ordered regions, and lower (<0.7) or negative NOE values indicate high conformational flexibility in the picosecond to nanosecond timescale. Overall, NOE values for PRM^{NS1} were lower than those for the nSH3 domain (Figs. 5 *A* and S7). Interestingly, even the residues in the PRM-binding surface of the nSH3 domain showed higher NOE values than the bound PRM^{NS1}. This feature has been observed in other

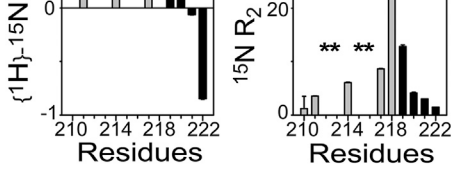

FIGURE 5 (*A*) {^{1}H}-^{15}N heteronuclear NOE and (*B*) ^{15}N R$_2$ of PRM^{NS1} in the complexed state. The asterisks represent the positions of Pro. The solid circles represent the positions of the residues whose peak intensities are too weak to measure. Black bars correspond to the C-terminal residues showing different conformations in the two crystal structures.

fuzzy complexes (15,33) in which a bound IDP/IDR retains high conformational flexibility on the surface of a rigid protein. Although the residues in the core PPLPPK sequence showed relatively high NOE values (~0.65), the N- and C-terminal residues were highly disordered (NOE < 0.4). These results indicate that the nSH3:PRM^{NS1} complex is a partial fuzzy complex, in which the bound PRM^{NS1} is relatively rigid in the core region but highly flexible in the terminal regions.

We also observed that the bound PRM^{NS1} is flexible in microsecond to millisecond timescales. At 25°C, the ^{15}N NMR R$_2$ values of K217, Q218, and K219 of PRM^{NS1} were noticeably elevated compared to those of other residues. The elevated R$_2$ value indicates the presence of conformational dynamics of bound PRM^{NS1} in microsecond to millisecond timescales (Fig. 5 *B*) (34). In particular, the linewidth of Q218 was severely broadened such that accurate measurement of its R$_2$ value was not possible. This is consistent with the structural heterogeneity of this region observed in the crystal structures. Hence, exchange between the two conformations PRM^{NS1A} and PRM^{NS1B} might be responsible for the elevated R$_2$ values.

The elevated R$_2$ values are not due to the on-off process of PRM^{NS1} to the nSH3 domain because R$_2$ values of the PRM^{NS1} binding sites in the nSH3 domain are not affected (Fig. S6). Our previous study has shown that the binding-unbinding processes of PRM^{NS1} induces significant NMR line broadening in the nSH3 domain (11). However, we cannot exclude the possibility that unidentified conformations are involved in mediating the conformational exchange processes. These results indicate that conformation of PRM^{NS1} is highly dynamic over broad timescales ranging from picoseconds to milliseconds.

To further elucidate the conformational dynamics of PRM^{NS1} in the bound state, we performed two all-atom 100 ns MD simulations, each using one of the crystal structures as the starting structure (Fig. 6). The two simulations did not converge well with each other during the 100 ns simulation time, indicating that the conversion between the two PRM^{NS1} conformations is slower than the simulation timescale. This is because the conversion requires large

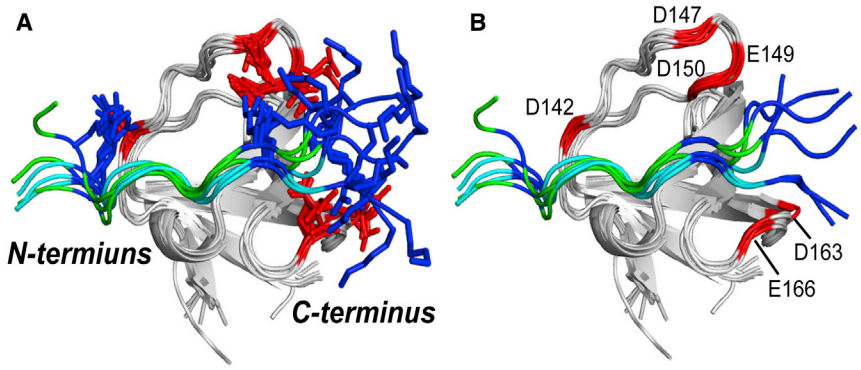

FIGURE 6 MD simulations of the nSH3: PRM^{NS1} complexes. In (*A*), representative PRM^{NS1} structures were selected from cluster analysis (see Materials and Methods) of the MD trajectories using PRM^{NS1A} (*green*) and PRM^{NS1B} (*cyan*). The positively and negatively charged residues are shown in blue and red, respectively. Side chains were omitted in (*B*) for clarity. To see this figure in color, go online.

changes in the φ/ψ angles of Q218 associated with breakage and reformation of multiple interactions, such as $E166^{nSH3}$-$Q218^{PRMNS1}$ and $E149^{nSH3}$-$R220^{PRMNS1}$. Consistent with this, R220 formed a stable hydrogen bond with $E149^{nSH3}$ with 89% occupancy in the simulation of PRM^{NS1B}, whereas it did not form in the simulation of PRM^{NS1A}. The occupancy of $E166^{nSH3}$-$Q218^{PRMNS1}$ interaction was 17% and 64% in the simulation of PRM^{NS1A} and PRM^{NS1B}, respectively. These results are consistent with our NMR data, indicating that N- and C-terminal regions undergo conformational exchanges in the microsecond to millisecond timescale.

Effects of structural disorder of bound PRM on long-range electrostatic interactions with the nSH3 domain

It was proposed that the polyelectrostatic model explains the thermodynamic contribution of long-range electrostatic interactions in a fuzzy complex (15). According to the model, K_d decreases exponentially as the net charge of a disordered ligand increases. We have previously shown that the binding affinity between the nSH3 domain and PRMs depends exponentially on the net charge of PRM (11). However, the bound PRM^{NS1} is partially fuzzy in that its terminal regions are highly flexible and its core PxxP sequence is relatively rigid. Thus, it remains to be determined whether the partial fuzziness of the bound PRM^{NS1} increases the multiplicity of long-range electrostatic interactions with the nSH3 domain as assumed in the polyelectrostatic model. This is an important question because many fuzzy complexes might be partially fuzzy.

However, it is difficult to test whether the structural disorder increases the number of long-range electrostatic interactions because there is no straightforward experimental method to tune the conformational flexibility of the bound ligand. As an alternative approach, we compared the number of long-range electrostatic interactions between MD trajectories and crystal structures that represent mobile and static states of the bound PRM^{NS1}, respectively.

We first identified acidic residues in the nSH3 domain that are involved in electrostatic interactions with the positive charges in the bound PRM^{NS1} by measuring changes in the side-chain carboxyl carbon chemical shifts ($^{13}C^{\gamma/\delta}O$) of all acidic residues in the nSH3 domain between the free and complexed states. This analysis identified six acidic residues (D142, D147, E149, D150, D163, and E166) (Fig. 7 *A*) that are located in and around the PRM^{NS1}-binding interface in the nSH3 domain (Fig. 7 *B*). Next, we measured the mean pairwise distances between the acidic residues in the nSH3 domain and positively charged residues in PRM^{NS1} in our MD simulations and in the two

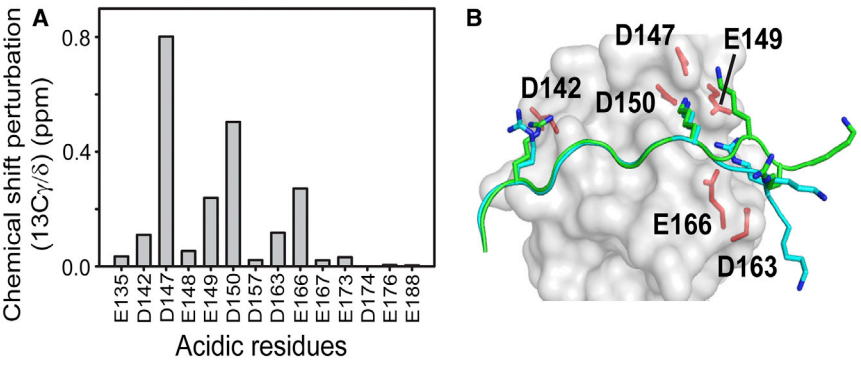

FIGURE 7 Detection of long-range electrostatic interactions between the nSH3 domain and PRM^{NS1} using NMR spectroscopy. (*A*) shows the $^{13}C^{\gamma/\delta}$ chemical shift perturbations of all acidic residues in the nSH3 domain upon the binding of PRM^{NS1}. (*B*) gives the positions of acidic residues whose $^{13}C^{\gamma/\delta}$ chemical shifts are perturbed noticeably. Overlaid structures of PRM^{NS1A} (*green*) and PRM^{NS1B} (*cyan*) are shown. To see this figure in color, go online.

TABLE 1 Differences in Average Pairwise Distances between MD and Crystal Structures

	Difference in Average Pairwise Distances (MD[a]–Crystal[b]) (Å)					
	Acidic Residues in the nSH3 Domain					
Residues in PRM^{NS1}	D142	D147	E149	D150	D163	E166
R211	negative 0.9	–[c]	–[c]	–[c]	–[c]	–[c]
K219	–[c]	negative 2.3	negative 1.3	negative 2.2	0.9	negative 0.5
R220	–[c]	negative 1.0	negative 0.4	negative 0.8	negative 1.1	negative 2.2
K221	–[c]	negative 3.4	negative 0.9	negative 1.5	3.8	negative 0.4

[a]Average distances of MD simulations of PRM^{NS1A} and PRM^{NS1B}.
[b]Average distances of two crystal structures (PRM^{NS1A} and PRM^{NS1B}).
[c]These distances were longer than 15 Å and were not included in the calculation.

crystal structures (Table S2). In this analysis, K217 in PRM^{NS1} was excluded because it is involved in well-defined short-range electrostatics, which are also present in other nSH3:PRM complexes. Interestingly, the mean pairwise distances calculated from the MD trajectories were considerably shorter than those calculated from the crystal structures (Table 1; Table S2). One obvious exception in Table 1 was the distance between K221 in PRM^{NS1} and D163 in the nSH3 domain, which is shorter in the crystal structures because of the lattice contacts around K221. The distance would be longer without the lattice contacts. These results indicate that partial disorder of the bound PRM^{NS1} increases the number of long-range electrostatic interactions, as was assumed in the polyelectrostatic model.

Although the polyelectrostatic model was developed to understand the binding mechanism of a fully fuzzy complex, its validity for partially fuzzy complex has not rigorously tested. Many IDP/IDR mediated complexes may be partially rather than fully disordered. Therefore, our results provide mechanistic insights into the role of nonspecific, long-range electrostatic interactions in other partially fuzzy complexes as well.

CONCLUSIONS

Many viral proteins interact with host modular binding domains such as SH3 domains by mimicking the cellular linear binding motifs (35,36). Although cellular PRMs bind to their cognate SH3 domains with weak affinities (K_d ~10 μM) (11,12,37), viral PRMs often show significantly higher affinities to the target SH3 domains (11,38,39). Both viral and cellular PRMs contain conserved core PxxP motif, but peripheral sequences in viral PRMs contain more charged residues than the ones in the cellular PRMs (38–40). Our study highlights that the pandemic IAV NS1 hijacks cellular CRK by exploiting the long-range electrostatic interactions mediated by the disordered peripheral region of its PRM. Recently, it was indicated that the amphiphysin-2 SH3 domain and PRM in NS3 of the Chikungunya virus bind via polyelectrostatic interactions mediated by the positively charged disordered region in the PRM (38). Interestingly, the binding affinity of this complex was also high (K_d = 24 nM). It is of interest that both viral proteins employ a similar strategy to hijack host signaling proteins containing SH3 domains. Therefore, it is likely that conformational dynamics within a complex are closely related to the functional roles of many SH3:PRM complexes (41). We anticipate that elucidating the molecular mechanisms underlying the binding affinity and selectivity of SH3:PRM interactions will help us understand host protein-protein interactions and design an inhibitor of viral infections.

SUPPORTING MATERIAL

Seven figures and two tables are available at http://www.biophysj.org/biophysj/supplemental/S0006-3495(18)30190-5.

AUTHOR CONTRIBUTIONS

J.-H.C. conceived the research. Q.S., D.Z., B.Z., P.L., and J.-H.C. conducted experiments. J.S. and W.H. conducted MD simulations. J.-H.C. and W.H. wrote the manuscript. All authors reviewed the manuscript.

ACKNOWLEDGMENTS

Work in the Cho lab was supported by start-up funds from Texas A&M University.

REFERENCES

1. Rubin, G. M., M. D. Yandell, …, S. Lewis. 2000. Comparative genomics of the eukaryotes. *Science.* 287:2204–2215.
2. Li, S. S.-C. 2005. Specificity and versatility of SH3 and other proline-recognition domains: structural basis and implications for cellular signal transduction. *Biochem. J.* 390:641–653.
3. Theillet, F.-X., L. Kalmar, …, V. N. Uversky. 2013. The alphabet of intrinsic disorder: I. Act like a Pro: On the abundance and roles of proline residues in intrinsically disordered proteins. *Intrinsically Disord. Proteins.* 1:e24360.
4. Dyson, H. J., and P. E. Wright. 2005. Intrinsically unstructured proteins and their functions. *Nat. Rev. Mol. Cell Biol.* 6:197–208.
5. Mittag, T., L. E. Kay, and J. D. Forman-Kay. 2010. Protein dynamics and conformational disorder in molecular recognition. *J. Mol. Recognit.* 23:105–116.

6. Uversky, V. N. 2015. Functional roles of transiently and intrinsically disordered regions within proteins. *FEBS J.* 282:1182–1189.
7. Tompa, P., and M. Fuxreiter. 2008. Fuzzy complexes: polymorphism and structural disorder in protein-protein interactions. *Trends Biochem. Sci.* 33:2–8.
8. Krug, R. M. 2015. Functions of the influenza A virus NS1 protein in antiviral defense. *Curr Opin Virol.* 12:1–6.
9. Finkelstein, D. B., S. Mukatira, …, C. W. Naeve. 2007. Persistent host markers in pandemic and H5N1 influenza viruses. *J. Virol.* 81:10292–10299.
10. Heikkinen, L. S., A. Kazlauskas, …, K. Saksela. 2008. Avian and 1918 Spanish influenza a virus NS1 proteins bind to Crk/CrkL Src homology 3 domains to activate host cell signaling. *J. Biol. Chem.* 283:5719–5727.
11. Shen, Q., D. Zeng, …, J. H. Cho. 2017. The molecular mechanisms underlying the hijack of host proteins by the 1918 Spanish influenza virus. *ACS Chem. Biol.* 12:1199–1203.
12. Bhatt, V. S., D. Zeng, …, J. H. Cho. 2016. Binding mechanism of the N-terminal SH3 domain of CrkII and proline-rich motifs in cAbl. *Biophys. J.* 110:2630–2641.
13. Shammas, S. L., M. D. Crabtree, …, J. Clarke. 2016. Insights into coupled folding and binding mechanisms from kinetic studies. *J. Biol. Chem.* 291:6689–6695.
14. Zhou, H. X., X. Pang, and C. Lu. 2012. Rate constants and mechanisms of intrinsically disordered proteins binding to structured targets. *Phys. Chem. Chem. Phys.* 14:10466–10476.
15. Borg, M., T. Mittag, …, H. S. Chan. 2007. Polyelectrostatic interactions of disordered ligands suggest a physical basis for ultrasensitivity. *Proc. Natl. Acad. Sci. USA.* 104:9650–9655.
16. Collaborative Computational Project, Number 4. 1994. The CCP4 suite: programs for protein crystallography. *Acta Crystallogr. D Biol. Crystallogr.* 50:760–763.
17. Adams, P. D., P. V. Afonine, …, P. H. Zwart. 2010. PHENIX: a comprehensive Python-based system for macromolecular structure solution. *Acta Crystallogr. D Biol. Crystallogr.* 66:213–221.
18. Emsley, P., and K. Cowtan. 2004. Coot: model-building tools for molecular graphics. *Acta Crystallogr. D Biol. Crystallogr.* 60:2126–2132.
19. Dolinsky, T. J., P. Czodrowski, …, N. A. Baker. 2007. PDB2PQR: expanding and upgrading automated preparation of biomolecular structures for molecular simulations. *Nucleic Acids Res.* 35:W522–W525.
20. Dolinsky, T. J., J. E. Nielsen, …, N. A. Baker. 2004. PDB2PQR: an automated pipeline for the setup, execution, and analysis of Poisson-Boltzmann electrostatics calculations. *Nucleic Acids Res.* 32:W665–W667.
21. Baker, N. A., D. Sept, …, J. A. McCammon. 2001. Electrostatics of nanosystems: application to microtubules and the ribosome. *Proc. Natl. Acad. Sci. USA.* 98:10037–10041.
22. Findeisen, M., T. Brand, and S. Berger. 2007. A 1H-NMR thermometer suitable for cryoprobes. *Magn. Reson. Chem.* 45:175–178.
23. Delaglio, F., S. Grzesiek, …, A. Bax. 1995. NMRPipe: a multidimensional spectral processing system based on UNIX pipes. *J. Biomol. NMR.* 6:277–293.
24. Keller, R. 2004. The Computer Aided Resonance Assignment Tutorial. CANTINA Verlag, Goldau, Switzerland.
25. Ferrage, F., A. Reichel, …, R. Ghose. 2010. On the measurement of ^{15}N-^{1}H nuclear Overhauser effects. 2. Effects of the saturation scheme and water signal suppression. *J. Magn. Reson.* 207:294–303.
26. Brooks, B. R., C. L. Brooks, 3rd, …, M. Karplus. 2009. CHARMM: the biomolecular simulation program. *J. Comput. Chem.* 30:1545–1614.
27. Hart, K., N. Foloppe, …, A. D. J. Mackerell, Jr. 2012. Optimization of the CHARMM additive force field for DNA: Improved treatment of the BI/BII conformational equilibrium. *J. Chem. Theory Comput.* 8:348–362.
28. Im, W., M. S. Lee, and C. L. Brooks, 3rd. 2003. Generalized born model with a simple smoothing function. *J. Comput. Chem.* 24:1691–1702.
29. Shao, J., S. W. Tanner, …, T. E. Cheatham. 2007. Clustering molecular dynamics trajectories: 1. characterizing the performance of different clustering algorithms. *J. Chem. Theory Comput.* 3:2312–2334.
30. Wu, X., B. Knudsen, …, J. Kuriyan. 1995. Structural basis for the specific interaction of lysine-containing proline-rich peptides with the N-terminal SH3 domain of c-Crk. *Structure.* 3:215–226.
31. Han, B., Y. Liu, …, D. S. Wishart. 2011. SHIFTX2: significantly improved protein chemical shift prediction. *J. Biomol. NMR.* 50:43–57.
32. Cavanagh, J., W. J. Fairbrother, …, N. J. Skelton. 2007. Protein NMR Spectroscopy. Elsevier Academic Press, Burlington, MA.
33. Sharma, R., Z. Raduly, …, M. Fuxreiter. 2015. Fuzzy complexes: specific binding without complete folding. *FEBS Lett.* 589 (19 Pt A): 2533–2542.
34. Palmer, A. G., 3rd, C. D. Kroenke, and J. P. Loria. 2001. Nuclear magnetic resonance methods for quantifying microsecond-to-millisecond motions in biological macromolecules. *Methods Enzymol.* 339:204–238.
35. Davey, N. E., G. Travé, and T. J. Gibson. 2011. How viruses hijack cell regulation. *Trends Biochem. Sci.* 36:159–169.
36. Duro, N., M. Miskei, and M. Fuxreiter. 2015. Fuzziness endows viral motif-mimicry. *Mol. Biosyst.* 11:2821–2829.
37. Ladbury, J. E., and S. Arold. 2000. Searching for specificity in SH domains. *Chem. Biol.* 7:R3–R8.
38. Tossavainen, H., O. Aitio, …, P. Permi. 2016. Structural basis of the high affinity interaction between the alphavirus nonstructural protein-3 (nsP3) and the SH3 domain of amphiphysin-2. *J. Biol. Chem.* 291:16307–16317.
39. Shelton, H., and M. Harris. 2008. Hepatitis C virus NS5A protein binds the SH3 domain of the Fyn tyrosine kinase with high affinity: mutagenic analysis of residues within the SH3 domain that contribute to the interaction. *Virol. J.* 5:24.
40. Arold, S., P. Franken, …, C. Dumas. 1997. The crystal structure of HIV-1 Nef protein bound to the Fyn kinase SH3 domain suggests a role for this complex in altered T cell receptor signaling. *Structure.* 5:1361–1372.
41. Stollar, E. J., H. Lin, …, J. D. Forman-Kay. 2012. Differential dynamic engagement within 24 SH3 domain: peptide complexes revealed by co-linear chemical shift perturbation analysis. *PLoS One.* 7:e51282.

Biophysical Journal, Volume *114*

Supplemental Information

Molecular Mechanisms of Tight Binding through Fuzzy Interactions

Qingliang Shen, Jie Shi, Danyun Zeng, Baoyu Zhao, Pingwei Li, Wonmuk Hwang, and Jae-Hyun Cho

Table S1. X-ray diffraction and refinement statistics for nSH3-PRM^{NS1} complex.

	6ATV.PDB
Data collection	
Space group	$P6_122$
Cell dimensions	
a, *b*, *c* (Å)	39.84, 39.84, 171.95
α, β, γ (°)	90.0, 90.0, 120.0
Resolution (Å)	1.75 (1.78 to 1.75)
R_{merge}	10.2% (23.3%)
$I / \sigma I$	16.8 (3.5)
Completeness (%)	94.9 (67.0)
Redundancy	12.0 (3.3)
Refinement	
Resolution (Å)	1.75
No. Reflections	8437
R_{work}/R_{free}	0.184/0.205
No. atoms	721
Protein	493
Ligand	114
Water	114
B-factors	
Protein	18.8
Ligand	18.8
Water	32.8
r.m.s. deviations	
Bond lengths (Å)	0.006
Bond angles (°)	0.781

* Values in parentheses are for the highest-resolution shells.

Table S2-1. The difference in average pairwise distances.

Residues in PRM^{NS1}	Difference in average pairwise distances (MD[a] - Crystal[b]) (Å)					
	Acidic residues in nSH3 domain					
	D142	D147	E149	D150	D163	E166
R211	0.0	-[c]	-[c]	-[c]	-[c]	-[c]
K219	-[c]	1.5	1.3	0.5	-0.2	0.7
R220	-[c]	-1.4	-1.3	-2.6	-5.4	-5.4
K221	-[c]	-1.3	1.8	-0.0	2.6	-0.5

[a]MD trajectories of PRM^{NS1A}
[b]Crystal structure of PRM^{NS1A} (PDB ID: 5UL6)
[c]These distances were longer than 15 Å and not included in the analysis.

Table S2-2. The difference in average pairwise distances.

Residues in PRM^{NS1}	Difference in average pairwise distances (MD[a] - Crystal[b]) (Å)					
	Acidic residues in nSH3 domain					
	D142	D147	E149	D150	D163	E166
R211	-1.7	-[c]	-[c]	-[c]	-[c]	-[c]
K219	-[c]	-6.1	-4.0	-4.9	1.9	-1.6
R220	-[c]	-0.6	0.5	1.1	3.2	0.9
K221	-[c]	-5.6	-3.6	-3.0	5.0	-0.3

[a]MD trajectories of PRM^{NS1B}
[b]Crystal structure of PRM^{NS1B} (PDB ID: 6ATV)
[c]These distances were longer than 15 Å and not included in the analysis.

Figure S1

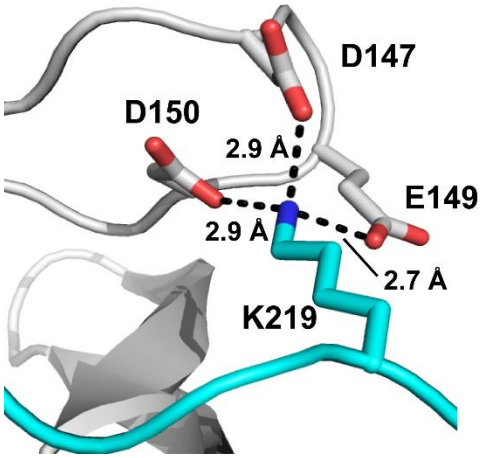

Figure S1. (A) The complex contains short-range electrostatic interactions between K217 of PRM^{NS1} and three acidic residues (D147, E149, and D150) in the nSH3 domain (PDB ID: 6ATV). The distances in the figure were measured between N^{ζ} of K219 and $O^{\delta/\varepsilon}$ of the acidic residues.

Figure S2

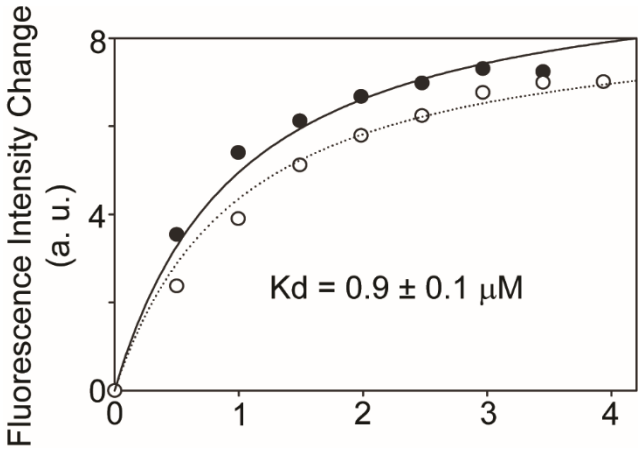

Figure S2. Fluorescence-based measurement of binding affinity between the nSH3 domain and mutant PRM^{NS1}, in which three C-terminal positively charged residues (K219-R220-K221) are replaced by Gly. The K_d value is from two repeated measurements.

Figure S3.

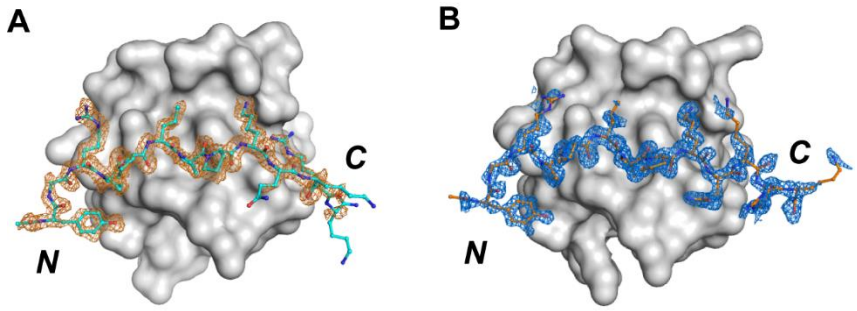

Figure S3. σA weighted $F_o - F_c$ map (contoured at 2σ) of (A) PRM^{NS1B} and (B) PRM^{NS1A}.

Figure S4.

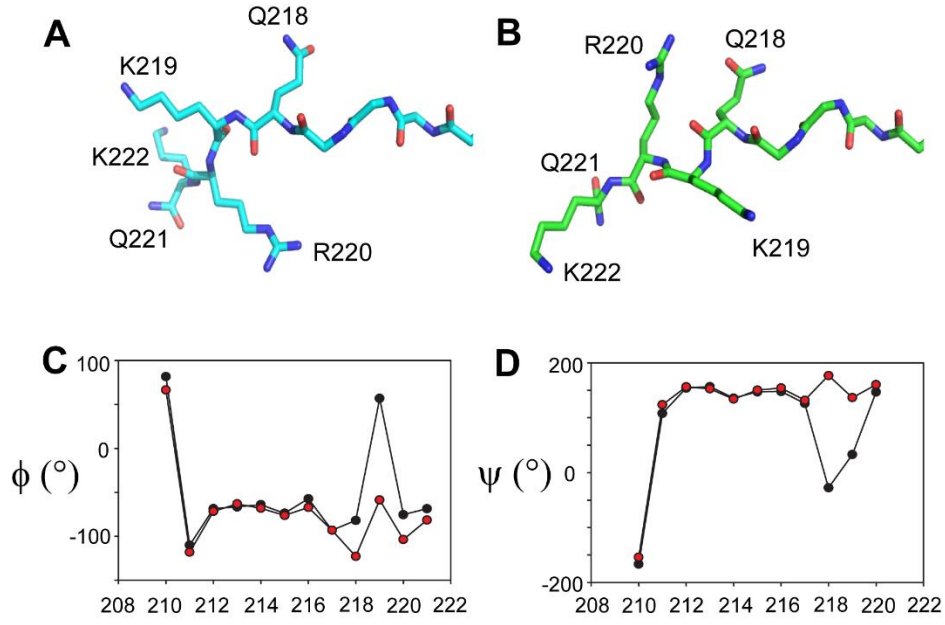

Figure S4. Conformational difference in the C-terminal region of the bound (A) PRM^{NS1B} and (B) PRM^{NS1A}. Significant changes in backbone (C) ϕ and (D) ψ angles of Q218 induced large changes in the conformations of positively charged residues in the C-terminal end of Q218.

Figure S5

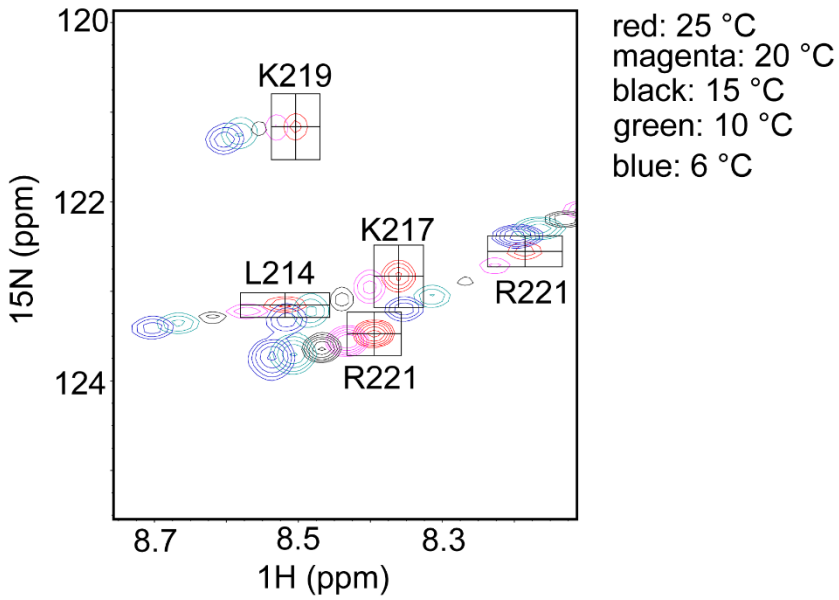

Figure S5. An overlay of temperature-dependent chemical shift changes for the C-terminal positively charged residues (K217, K219, R220, and K221) in PRM^{NS1}.

Figure S6

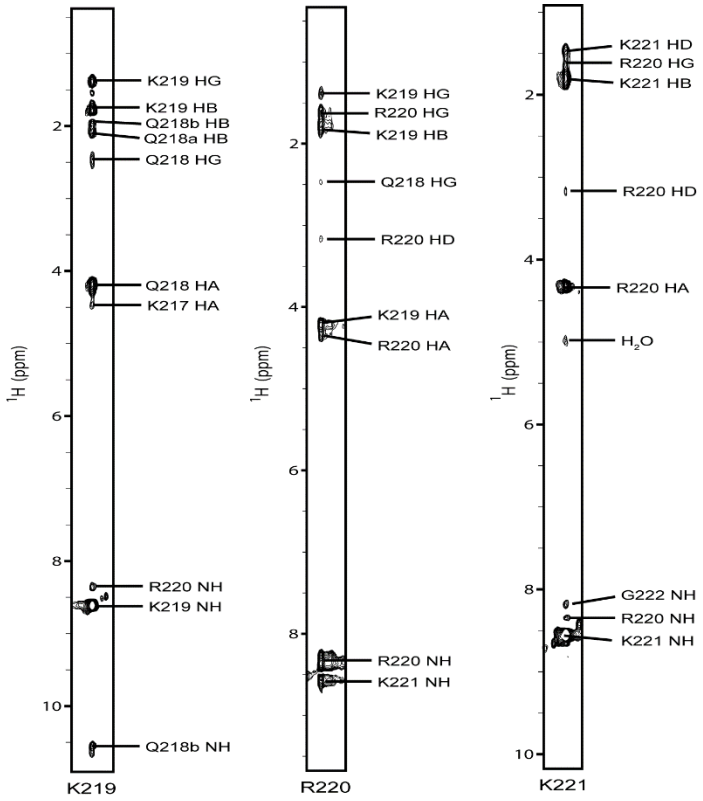

Figure S6. ^{15}N-edited NOESY HSQC of the C-terminal positively charged residues (K219, R220, and K221) in PRM^{NS1} bound to the nSH3 domain. The data was acquired using a sample of ^{15}N-labeled PRM^{NS1} saturated by non-labeled nSH3 domain. The NOESY mixing time was 100 ms.

Figure S7

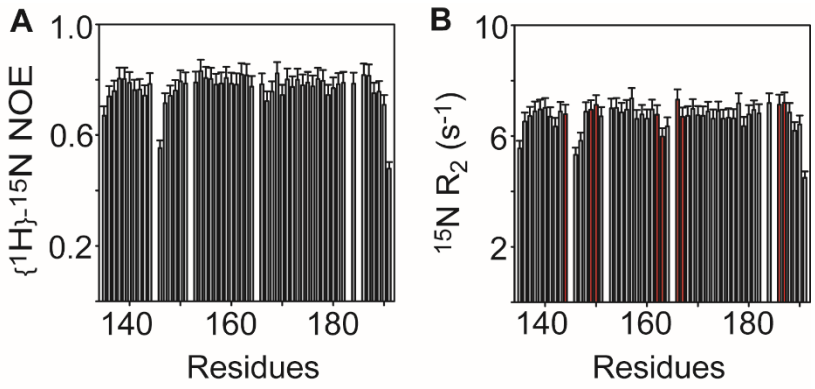

Figure S7. (A) {^{1}H}-^{15}N heteronuclear NOE and (B) ^{15}N R_2 of the nSH3 domain saturated by PRM^{NS1}. Red bars represent the residues in the nSH3 domain that are in the binding interface with PRM^{NS1}. This represents that the elevated R_2 in PRM^{NS1} is not induced by its on-off process.